Progress In Electromagnetics Research B, Vol. 15, 307–324, 2009

PATCH SHAPE INFLUENCE UPON RADAR CROSS SECTION OF A CYLINDRICAL MICROSTRIP ANTENNA

A. Y. Svezhentsev and V. V. Kryzhanovskiy

The A. Ya. Usikov Institute of Radio Physics and Electronics
The National Academy of Sciences of Ukraine
12, Akad. Proskury Str., Kharkov 61085, Ukraine

Abstract—The patch shape influence on the radar cross section (RCS) of a cylindrical microstrip antenna (CMA) is discussed. The RCS of the CMA is evaluated from a plane wave scattering problem solution to a cylindrical microstrip antenna. The method of moments is employed in the spectral domain using sub-domain basis functions. It is shown that the patch shape has a pronounced effect such that new resonance modes appear at frequencies substantially shifted towards the low-frequency end compared to a cylindrical rectangular patch.

1. INTRODUCTION

Widely accepted in mobile and satellite communications, cylindrical microstrip antennas (CMA) have long been an area of intensive research. Over the recent decades, the CMA characteristics have been thoroughly studied in a variety of ways [1–13]. The method of moments [5–13] employed in both spectral [6–9] and spatial domains [5, 10–13] is most universal. But introducing the basis functions on the entire patch area (entire domain basis functions) [5, 6, 9] allows dealing with rectangular cylindrical patches only. Arbitrarily configured patches require using sub-domain basis functions. Examples are shown in papers [7, 8, 10–13], where the excitations are a cylindrical microstrip line [7, 8, 13], a probe [10, 12] and a plane wave [11]. Works [7, 8, 10–13] focuse on such characteristics as the CMA input impedance versus frequency, radiation pattern at a fixed frequency and, also, the far field at a fixed frequency in a specific direction, which is similar to radar cross section (RCS).

Corresponding author: A. Y. Svezhentsev (svezh@kharkov.ua).

However, the only concern of papers [7, 8, 10–13] was rectangular cylindrical patches. A rare exception is papers [8] and [13] discussing the CMA with a recessed feed. So, the CMA characteristics in the case of complex shape patches highly need investigation.

The present paper seeks to examine the CMA radar cross section under patch shape changes caused by the introduction of complex-shape slots. The study will be completed with patch current density distributions at resonance frequencies. Patch shapes of the present concern have never been studied. Here, as in [7, 8], the problem will be solved by the method of moments in the spectral domain with sub-domain basis functions. The difference consists in the employment of piecewise sinusoidal basis functions (PWS) rather than rooftops in [7, 8]. Besides, the Fourier integrals will be taken on the real axis rather than over a complex-plane contour, and surface wave contributions will be extracted as single terms.

2. EVALUATION OF CMA RADAR CROSS SECTION

Refer to the CMA model given in Fig. 1. The metal patch is placed on the external interface of the so-called Goubau line [14], a z-infinite circular metal cylinder having radius r_1 and surrounded by a circular dielectric substrate of radius r_0 and related permittivity ε_r. The patch is arbitrarily shaped in the context of rectangular cylindrical geometry. The shapes to consider are sketched in Fig. 2.

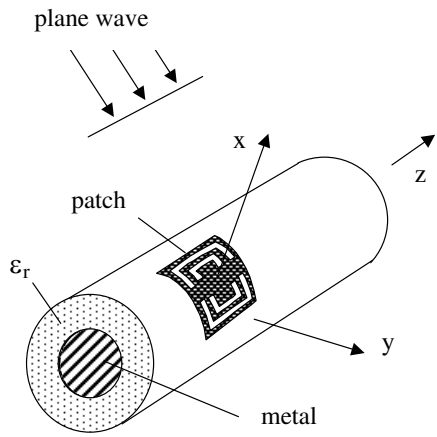

Figure 1. The plane wave excitation of a cylindrical microstrip antenna with an arbitrarily shaped patch.

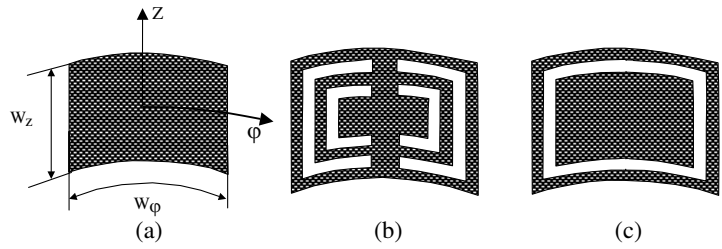

Figure 2. Patch configurations: (a) Rectangular cylindrical, (b) with four U-shaped slots, and (c) with a looped slot.

Let the plane wave

$$\mathbf{E}^{inc} = \mathbf{E}^0 e^{ik_0(\vec{n}\vec{R})} \tag{1}$$

arrive from infinity in the n direction as shown in Fig. 3. In what follows, the time dependence $e^{i\omega t}$ will be omitted. In a cylindrical coordinate system, the z-components of the electric and magnetic fields of the incident unit-amplitude plane wave are written as follows [15]

$$E_z^{inc}(r,\varphi,z) = \sum_{n=-\infty}^{n=\infty} a_{nz}(r,z)e^{-in(\varphi-\beta)}, \tag{2}$$

$$H_z^{inc}(r,\varphi,z) = \sum_{n=-\infty}^{n=\infty} \bar{a}_{nz}(r,z)e^{-in(\varphi-\beta)}, \tag{3}$$

with

$$a_{nz}(r,z) = w_0\cos(\gamma)\sin(\alpha)e^{-ik_0 z\cos\alpha}i^n J_n(k_0 r\sin\alpha)$$

$$\bar{a}_{nz}(r,z) = w_0\sin(\gamma)\sin(\alpha)e^{-ik_0 z\cos\alpha}i^n J_n(k_0 r\sin\alpha),$$

where W_0 is the free space wave impedance; $J_n(x)$ is the Bessel function; γ is the polarization parameter; $k_0 = 2\pi/\lambda_0$; and λ_0 is the free space wavelength. The angles α and β specify the wave incidence direction (Fig. 3). The problem consists in finding the patch current distribution induced by the incident field.

In accordance with the equivalence theorem [16], the metal patch is replaced by the equivalent electric surface current (sheet electric current) distributed over the metal patch surface S'. The current density $\mathbf{J}_s^e(r_0,\varphi',z')$ is unknown; subscript s stands for z,φ. Then the total tangential electric field can be written as a sum of the excitation

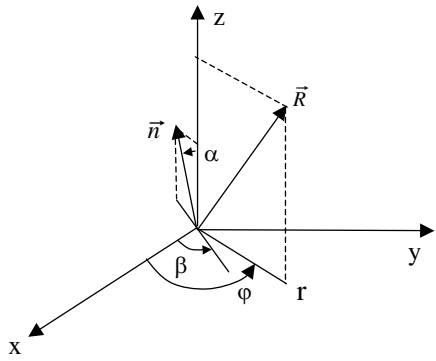

Figure 3. The incidence field orientation angles with respect to the CMA coordinate system.

field caused by the incident field and the scattered field generated by the equivalent surface current as follows

$$E_s^p(r,\varphi,z) = E_s^{p,exc}(r,\varphi,z) + E_s^{scat,J}(r,\varphi,z), \tag{4}$$

with

$$\mathbf{E}_s^{scat,J}(r,z,\varphi) = \int\limits_{z'}\int\limits_{\varphi'} \begin{bmatrix} \mathbf{J}_z^e(r_0,\varphi',z') \\ \mathbf{J}_\varphi^e(r_0,\varphi',z') \end{bmatrix} \hat{\mathbf{G}}^J(r,r_0,z,z',\varphi,\varphi')dS' \tag{5}$$

where

$$\hat{\mathbf{G}}^J(r,r_0,z,z',\varphi,\varphi') = \begin{bmatrix} \mathbf{G}_{zz}^J(r,r_0,z,z',\varphi,\varphi') & \mathbf{G}_{z\varphi}^J(r,r_0,z,z',\varphi,\varphi') \\ \mathbf{G}_{\varphi z}^J(r,r_0,z,z',\varphi,\varphi') & \mathbf{G}_{z\varphi}^J(r,r_0,z,z',\varphi,\varphi') \end{bmatrix}$$

is the Green function; $\mathbf{J}_s^e$ is the unknown equivalent surface current density; index p marks one of the two introduced partial domains: $p = 0$ stands for $r > r_0$ and $p = 1$ for $r_0 > r > r_1$. The derivation of (5) is given in [6]. The excitation field is introduced as follows

$$\mathbf{E}_s^{0,exc}(r,\varphi,z) = \mathbf{E}_s^{inc}(r,\varphi,z) + \mathbf{E}_s^{0,scat,G}(r,\varphi,z) \tag{6}$$

$$\mathbf{E}_s^{1,exc}(r,\varphi,z) = \mathbf{E}_s^{1,scat,G}(r,\varphi,z). \tag{7}$$

The field $\mathbf{E}_s^{p,scat,G}(r,\varphi,z)$ is determined by the solution of the diffraction of plane wave (1) by the Goubau line (see Fig. 1). For this, refer, in particular, to [11]. In this problem formulation, the field $\mathbf{E}_s^{p,exc}(r,\varphi,z)$ satisfies the boundary conditions on the dielectric-air homogeneous interface and the boundary conditions on the circular

metal cylinder. The calculation formula of the excitation field introduced in (6), (7) is given in Appendix B. The application of the boundary condition that the total tangential electric field vanishes on the substituted metal patch surface yields the integral equation for the unknown surface current density

$$-\mathbf{E}_s^{0,exc}(r_0,z,\varphi)=\iint\limits_{z'\varphi'}\begin{bmatrix}\mathbf{J}_z^e(r_0,\varphi',z')\\ \mathbf{J}_\varphi^e(r_0,\varphi',z')\end{bmatrix}\hat{\mathbf{G}}^J(r,r_0,z,z',\varphi,\varphi')dS' \quad (8)$$

Integral equation (8) is solved by the method of moments under Galerkin's scheme. The unknown surface current density is expanded in the basis functions as follows

$$\mathbf{J}_s=\sum_{q=1}^{NB}\alpha_q\mathbf{J}_{qs}^b. \quad (9)$$

Here $\mathbf{J}_{qs}^b$ are the basis functions of the number $NB=NBZ+NB\varphi$, where $NBZ=(NZ-1)*N\varphi$ and $NB\varphi=(N\varphi-1)*NZ$, with NZ and $N\varphi$ being the numbers of patch divisions along the z and φ directions, respectively. Each segment size in the relevant direction is $\Delta_z=W_z/NZ$ and $\Delta_\varphi=W_\varphi/N\varphi$. The patch splitting into rectangular cylindrical segments is shown in Fig. 4. As seen, each basis function is given on two adjacent segments, for details see Appendix C. By the method of moments, integral equation (8) is reduced to the system of linear algebraic equations (SLAE)

$$\mathbf{Z}\boldsymbol{\alpha}=\mathbf{V} \quad (10)$$

where $\boldsymbol{\alpha}[i]=\alpha_i$. In the present paper, the elements of matrix $\mathbf{Z}$ are evaluated in the spectral domain as

$$Z_{ik}=\frac{1}{4\pi^2}\sum_{n=-\infty}^{\infty}\int\limits_{h=-\infty}^{\infty}\tilde{\mathbf{J}}_i^t(r_0,-n,-h)\hat{\tilde{\mathbf{G}}}^J(r_0,n,h)\tilde{\mathbf{J}}_k^b(r_0,n,h)dh, \quad (11)$$

where $\tilde{\mathbf{J}}^b(r_0,n,h)$, $\tilde{\mathbf{J}}^t(r_0,-n,-h)$, and $\hat{\tilde{\mathbf{G}}}^J(r_0,n,h)$ are the spectral equivalents of the values $\mathbf{J}_{qs}^b$, $\mathbf{J}_{qs}^t$, $\hat{\mathbf{G}}^J$, respectively, with $\mathbf{J}_{qs}^t$ being the test function. The elements of column $\mathbf{V}$ are calculated in the spatial domain as

$$V_i^s=-\iint\limits_{S_i}ds'\mathbf{J}_{is}^t\mathbf{E}_s^{0,exc}(r_0,z,\varphi), \quad (12)$$

S_i is the surface where the ith basis function is introduced. The spectral Green function $\hat{\tilde{\mathbf{G}}}^J(r_0, n, h)$ is available from Appendix A. To accelerate the evaluation of the matrix elements Z_{ik}, an expedient [7] was taken consisting in the subtraction and the addition of the Green function asymptotical representation. The Fourier transforms of the basis functions and the final formula for the calculation of the elements V_i^s are given in Appendix C.

The solution of SLAE (10) yields the current distribution on the patch. Hence, by virtue of (5), one finds the field at any point of space. The far field comes from the asymptotical evaluation of expression (5) [17]. Finally the field $\mathbf{E}_s^{scat,J}(r, z, \varphi)$ in the far zone appears to be a spherical wave of the form $\mathbf{E}^{scat,J}(R, \theta, \varphi)$. The far-field components are available, in particular, from [11]. Then the RCS is provided by the formula

$$\sigma_{uv} = \frac{4\pi \left|\mathbf{E}^{scat,J}(R, \theta = \pi - \alpha, \varphi = \beta) \cdot \mathbf{v}\right|^2}{\left|\mathbf{E}_u^0\right|^2}, \tag{13}$$

where $\mathbf{E}^{scat,J} \cdot \mathbf{v}$ is the v-component ($v = (\theta, \varphi)$) of the scattered field in the direction reverse to the plane wave arrival, i.e., in the $-\mathbf{n}$ direction.

3. NUMERICAL RESULTS

Before analyzing different patch shapes for RCS, take up the CMA structure with a rectangular cylindrical patch. Let the CMA

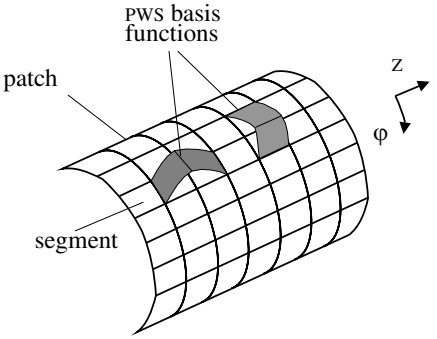

Figure 4. The patch surface splitting into segments and the introduction of the basis functions.

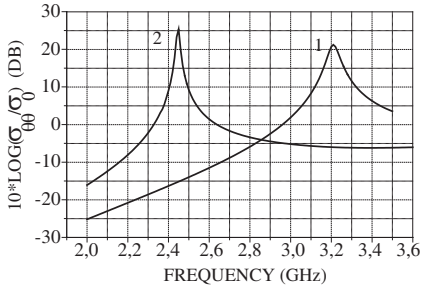

Figure 5. The radar cross section of a CMA with a rectangular cylindrical patch: $\sigma_{\theta\theta}/\sigma_0$ (Curve 1) and $\sigma_{\theta\theta}/\sigma_0$ (Curve 2).

parameters be the same as those in [4]. Specifically, $W_z = 3\,\text{cm}$, $W_\varphi = 4\,\text{cm}$, $r_1 = 0.05\,\text{m}$, $\varepsilon_r = 2.32$, and $r_0/r_1 = 1.0159$. The frequency dependences of $\sigma_{\theta\theta}/\sigma_0$ and $\sigma_{\varphi\varphi}/\sigma_0$ are shown in Fig. 5 (curves 1 and 2, respectively, dB), where $\sigma_0 = \pi W_z W_\varphi$ is the normalization parameter. The curves come from formula (13) and correspond to the plane wave normal incidence on the structure, i.e., $\alpha = 90°$ and $\beta = 0°$. This case refers to $\bar{h} = \cos(\alpha) = 0$ in Appendix A. Curve 1 corresponds to $\gamma = 0°$ (E-polarization, $E_z^{0,exc} \neq 0$, $H_z^{0,exc} = 0$) and Curve 2 is for $\gamma = 90°$ (H-polarization, $E_z^{0,exc} = 0$, $H_z^{0,exc} \neq 0$). In Fig. 5, two resonances are clearly seen at frequencies $f = 3.21\,\text{GHz}$ and $f = 2.45\,\text{GHz}$. For comparisons, the input impedance calculation results for the probe-fed CMA in [4] show resonances at 3.232 GHz and 2.449 GHz for the z- and φ-polarized patch, respectively. The resonance frequencies differ by less than 0.7% from those in work [4], indicating a very good agreement of the data. Fig. 6 plots the z-component of the electric current distribution (Curve 1 in Fig. 5) at resonance frequency $f = 3.21\,\text{GHz}$. This distribution fits the fundamental mode in the z-polarized patch case. Such a mode is excited right in the case of E-polarized plane wave incidence on the structure. For reference, the phase distribution of the electric current z-component of the above-mentioned fundamental mode is constant.

It is clear that the slot introduction into the metal patch can essentially affect the electric current distribution on the patch and,

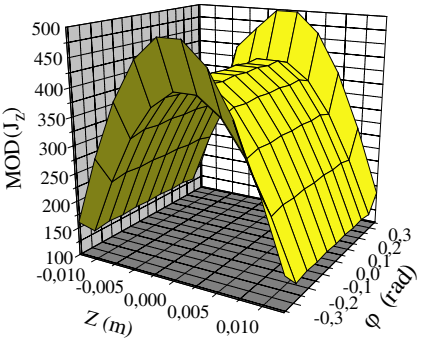

Figure 6. Distribution of the electric current z-component module on a rectangular cylindrical patch (see Fig. 2(a)).

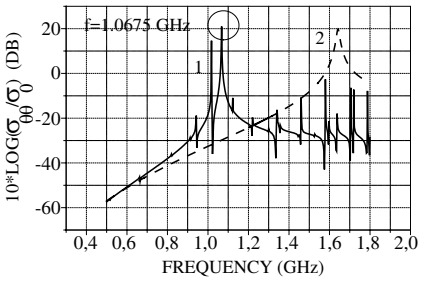

Figure 7. The radar cross section $\sigma_{\theta\theta}/\sigma_0$ of a CMA whose patch has four U-shaped slots (Curve 1) and a CMA with a rectangular cylindrical patch (Curve 2).

hence, the antenna RCS. In particular, a patch with a U-slot is known to offer a number of properties enhancing the planar printed (microstrip) antenna performance [18]. Take up a CMA with a patch with four U-slots (Fig. 2(b)) with the parameters $W_z = 4.9\,\text{cm}$, $W_\varphi = 6.5\,\text{cm}$, $r_1 = 0.05\,\text{m}$, $\varepsilon_r = 3.38$, and $r_0/r_1 = 1.0159$. In this situation, we split the original rectangular cylindrical patch (Fig. 4) into the $NZ \times N\varphi = 24 \times 34$ segments. Then some metal segments are removed to achieve the desired configuration (Fig. 2(b)). Let the CMA be exited by a normally incident E-polarized plane wave, i.e., $\alpha = 90°$, $\beta = 0°$, and $\gamma = 0°$. In the further consideration, these angles of the incident field orientation will be considered. The frequency dependence of $\sigma_{\theta\theta}/\sigma_0$ for the CMA with the above-mentioned patch (Fig. 2(b)) is plotted in Fig. 7, Curve 1. Curve 2 gives the $\sigma_{\theta\theta}/\sigma_0$ of a rectangular

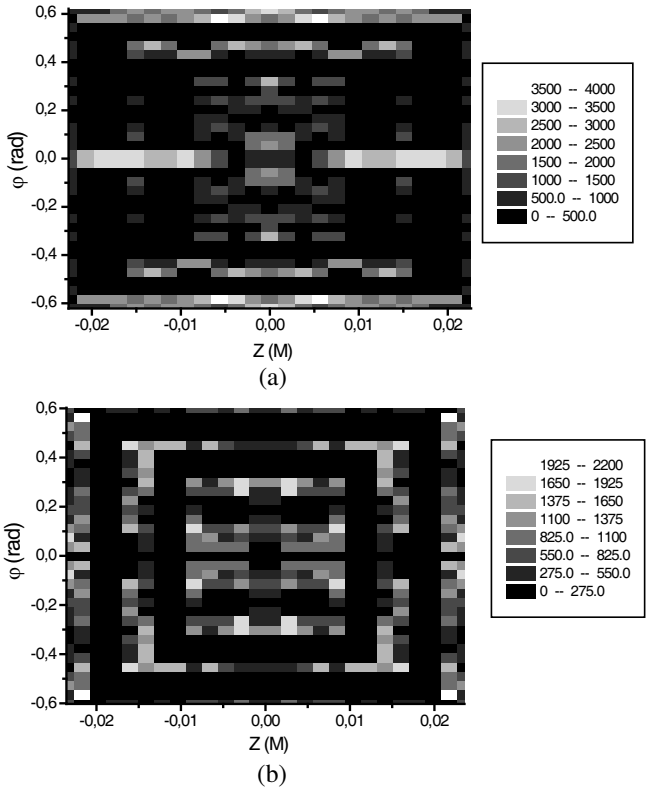

Figure 8. The $|J_z(z,\varphi)|$ (a) and $|J_\varphi(z,\varphi)|$ (b) distributions on a patch with four U-shaped slots. The brightest areas correspond to the highest amplitude.

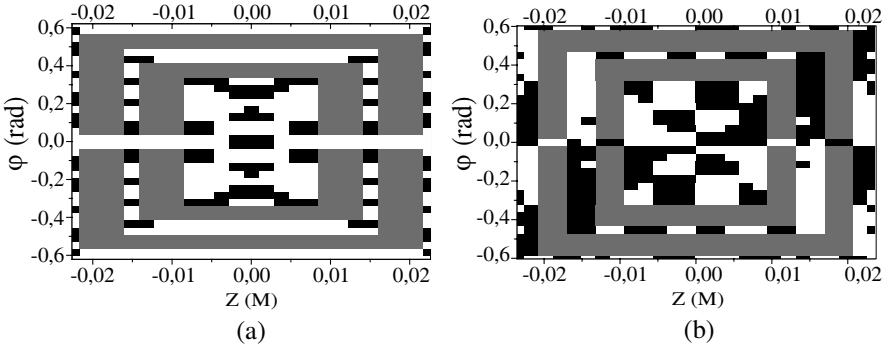

Figure 9. The phase $J_z(z,\varphi)$ (a) and $J_\varphi(z,\varphi)$ (b) distributions on a patch with four U-shaped slots. The phase difference between the white and the black spans 180°, the grey establishes slot positions.

cylindrical patch, demonstrating the fundamental resonance of a CMA with a rectangular cylindrical patch. Curve 1 is a representative of the fact that for E-polarized wave incidence, a patch with four U-slots has lots of resonances in the region where a rectangular cylindrical patch has a single one. Amongst these numerous resonances, the one at frequency $f = 1.0675\,\text{GHz}$ is evidently of primary interest, being the strongest, its band the widest. The surface current module distribution on a patch with four U-slots (Fig. 2(b)) is displayed in light and dark in Fig. 8(a) for $J_z(z,\varphi)$ and in Fig. 8(b) for $J_\varphi(z,\varphi)$, $f = 1.0675\,\text{GHz}$. The brightest areas correspond to the highest amplitude. The darkest areas establish slot positions and, also, zero amplitude spots. The maximum of the $J_z(z,\varphi)$ module is a little more than twice as large as the $J_\varphi(z,\varphi)$ module, which is attributed to the splitting of the J_z current into the two J_φ components at the points $z = \pm 0.021\,\text{m}$, $\varphi = 0$. The phase distributions of the patch surface currents $J_z(z,\varphi)$ and $J_\varphi(z,\varphi)$ at $f = 1.0675\,\text{GHz}$ are plotted in Figs. 9(a) and (b), respectively. The white to black spans a 180° phase difference, the grey shades locate the slots. The distribution of the electric current module density for this oscillation suggests that the current distribution on the metal patch is quite complex; the maximum current density falls on the patch central line at $\varphi = 0$. The analysis of the current density phase distribution (Figs. 9(a), (b)) indicates that the $J_z(z,\varphi)$ distribution is symmetrical about the plane $\varphi = 0$, while the $J_\varphi(z,\varphi)$ distribution is asymmetrical about $\varphi = 0$. In other words, while $J_z(z,\varphi)$ has a peak, $J_\varphi(z,\varphi)$ goes to zero in this plane. The examination of the amplitude and phase distributions of the patch surface current density (see Figs. 8 and 9) enables us to construct the distribution of the patch current density

vector conventionally shown in Fig. 10. Let us give a detailed physical analysis to this.

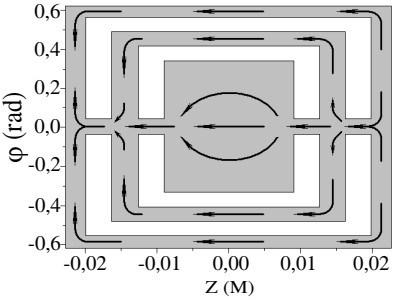

Figure 10. The vector of surface current density distribution on a patch with four U-slots.

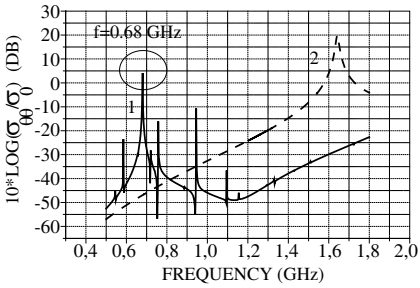

Figure 11. The radar cross section $\sigma_{\theta\theta}/\sigma_0$ of a CMA whose patch has a looped slot (Curve 1) and a CMA with a rectangular cylindrical patch (Curve 2).

The patch with four U-slots can be (on condition) composed of five horizontal (z-parallel) strip conductors (one of them makes an interior rectangle) and four vertical (φ-parallel) strip conductors. The excitation field induces cophasal currents on the five horizontal conductors. On the central conductor ($|z| \leq 0.01\,\text{m}$, $|\varphi| \leq 0.3$ radian), the currents are distributed over the whole surface, covering all its width when $|z| < 0.05\,\text{m}$. Inside the gaps between the slots ($|z| = 0.01\,\text{m}$, $\varphi = 0$ and $|z| = 0.015\,\text{m}$, $\varphi = 0$), the currents are concentrated into the J_z being at a maximum. At the ends of the linear conductor segments, the currents J_z transform to the J_φ, with the initial phase conserved. The behavior of the current J_φ is more complicated. Its distribution on the vertical conductors is not only asymmetric (with initial phase varying) about the plane $\varphi = 0$. It is remarkable that it changes its initial phase when passing from the central and the intermediate conductors ($|z| \leq 0.01\,\text{m}$ and $|z| = 0.015\,\text{m}$) to the outer vertical conductors at $\varphi = 0$. Also, the initial phase is changed at $|z| = 0.021\,\text{m}$, $|\varphi| = 0.32$ radian. As a result, J_φ vanishes at $|z| = 0.021\,\text{m}$, $|\varphi| = 0.32$ radian, and potential difference (voltage) loops take place at the points. The practical use of this fact consists in the following. When feeding this topology patch, the source energy must be halved and cophasally delivered to the points $z = 0.021\,\text{m}$, $\varphi = \pm 0.32$ radian or $z = -0.021\,\text{m}$, $\varphi = \pm 0.32$ radian.

Consider the CMA with a looped slot (Fig. 2(c). The $\sigma_{\theta\theta}/\sigma_0$ versus frequency is seen in Fig. 11, Curve 1. As before, Curve 2 is for

the $\sigma_{\theta\theta}/\sigma_0$ of a rectangular cylindrical patch. As in the previous case (see Fig. 7), the considered frequency region abounds with resonances. The highest quality resonance is at the frequency $f = 0.68\,\text{GHz}$. The patch current module and the phase distributions are in Figs. 12 and 13, respectively. The pictures suggest that for this oscillation type, the current is mainly concentrated round the patch perimeter, in the area outside the loop of the slot. The current density phase distribution (the color pattern and gradation are similar to Fig. 9) shows that the z-component of the current is symmetrical about the plane $\varphi = 0$, while the φ-component distribution is asymmetrical and vanishes in the $\varphi = 0$ plane.

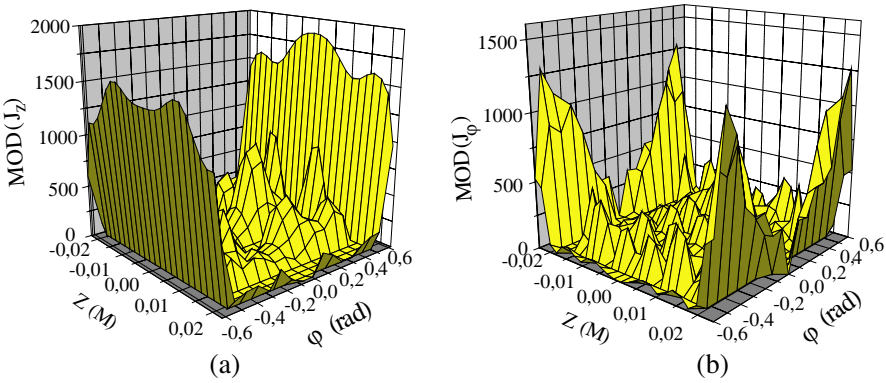

Figure 12. The $|J_z(z,\varphi)|$ (a) and $|J_\varphi(z,\varphi)|$ (b) distributions on a patch with a looped slot.

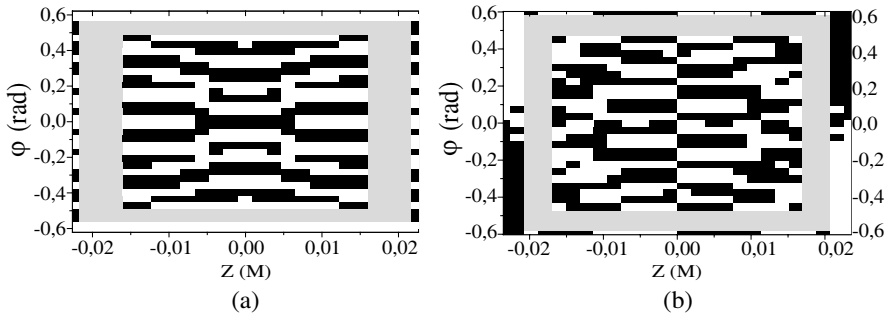

Figure 13. The phase $J_z(z,\varphi)$ (a) and $J_\varphi(z,\varphi)$ (b) distributions on a patch with a looped slot. The phase difference between the white and the black spans 180°, the grey establishes slot positions.

The vector of surface current density distribution on a patch with

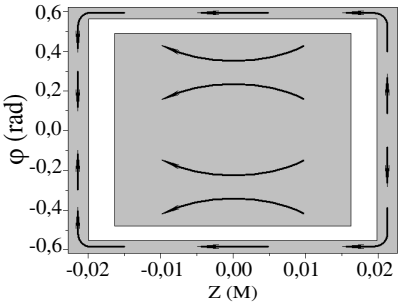

Figure 14. The vector of surface current density distribution on a patch with a looped slot (Fig. 2(c)).

a looped slot is sketched in Fig. 14. A peak of the potential difference is observed for $|z| = 0.021$ m, $\varphi = 0$, which allows this patch excitation with a lumped source. The current distribution in the middle of the patch oscillates with an alternating phase and small amplitude, making the contribution from these currents to the radiation field far less than it is from the exterior looped conductor. A brief summary as to the patches with four U-slots or a looped slot is that the related decrease of the resonance frequency of the fundamental oscillation is the more evident, the longer are conductors supporting the cophasal component of the current J_φ.

The obtained results suggest that for a CMA with an arbitrarily shaped patch (Figs. 2(b) and (c)), a series of high-Q resonances appear at lower frequencies compared to the fundamental resonance of a rectangular cylindrical patch. Specifically, for the E-polarized wave incidence, a rectangular cylindrical patch has a resonance at frequency $f = 1.6425$ GHz, while the resonance frequency of a patch with four U-slots (Fig. 2(b)) is $f = 1.0675$ GHz, and it is $f = 0.68$ GHz for a looped-slot patch (Fig. 2(c)).

4. CONCLUSION

The plane wave scattering problem of a cylindrical microstrip antenna with an arbitrarily shaped patch has been solved by the method of moments in the spectral domain using piecewise basis functions. A numerical algorithm for the radar cross section calculation has been developed. At the beginning, the radar cross section was calculated for a cylindrical microstrip antenna with a rectangular cylindrical patch. The resonance frequencies of the fundamental z- and φ-polarized oscillations are in a good agreement with the probe-fed antenna data available from the literature, suggesting that the developed algorithm

works well.

Then the radar cross section of a cylindrical microstrip antenna has been calculated for patches of different shapes. In particular, the consideration was given to patches with four U-slots or a looped slot. Amplitude and phase distributions of the current density at resonance frequencies have been evaluated and analyzed. It has been shown that resonance frequencies of a CMA with complex-shape patches can be at substantially lower frequencies compared to the configuration carrying a rectangular cylindrical patch.

The results presented in the paper for arbitrarily shaped patches, namely, locations of all the resonant frequencies and current distribution peculiarities can be directly used for same-shape patch antennas fed by other sources, such as a probe or a microstrip line.

APPENDIX A. THE SPECTRAL GREEN FUNCTIONS

The components of the Green function $\hat{\bar{\mathbf{G}}}^J(r_0, n, h)$ in the spectral domain take the following appearance [19]

$$\hat{\bar{\mathbf{G}}}^J(r_0, n, h) = \begin{bmatrix} \chi_{nzz}(r_0, \bar{h}) & \chi_{nz\varphi}(r_0, \bar{h}) \\ \chi_{n\varphi z}(r_0, \bar{h}) & \chi_{n\varphi\varphi}(r_0, \bar{h}) \end{bmatrix} \tag{A1}$$

where

$$\chi_{n(zz)}(r_0, \bar{h}) = -\frac{\Delta_n^H(\bar{h})}{\Delta_n(\bar{h})} \frac{w_0}{k_0 r_0};$$

$$\chi_{n(z\varphi)}(r_0, \bar{h}) = \chi_{n(\varphi z)}(r_0, \bar{h}) = iw_0 \bar{F}_n \frac{\bar{\Delta}_n(\bar{h})}{\Delta_n(\bar{h})} + \frac{n\bar{h}w_0}{x_1^2} \frac{\Delta_n^H(\bar{h})}{\Delta_n(\bar{h})};$$

$$\chi_{n(\varphi\varphi)}(r_0, \bar{h}) = -\frac{iw_0 n\bar{h}k_0 r_0}{x_0 x_1} \frac{\bar{\Delta}_n(\bar{h})}{\Delta_n(\bar{h})} \left[\frac{x_1}{x_0} \bar{F}_n(\bar{h}) + \frac{x_0}{x_1} \Phi_n(\bar{h}) \right]$$

$$-\frac{(n\bar{h})^2 w_0 k_0 r_0}{(x_0 x_1)^2} \frac{\Delta_0^H(\bar{h})}{\Delta_n(\bar{h})} + k_0 r_0 w_0 \Phi_n(\bar{h}) \bar{F}_n \frac{\Delta_n^E(\bar{h})}{\Delta_n(\bar{h})};$$

$$\bar{\Delta}_n(\bar{h}) = n\bar{h} \left[x_1^{-2} - x_0^{-2} \right]; \Delta_n^E(\bar{h}) = -i \left[\Phi_n(\bar{h}) - \varepsilon_{r1} F_n(\bar{h}) \right];$$

$$\Delta_n^H(\bar{h}) = i \left[\Phi_n(\bar{h}) - \bar{F}_n(\bar{h}) \right]; F_n(\bar{h}) = \frac{\gamma_1'(r_0)}{x_1 \gamma_1(r_0)}; \bar{F}_n(\bar{h}) = \frac{\bar{\gamma}_1'(r_0)}{x_1 \bar{\gamma}_1(r_0)};$$

$$\Phi_n(\bar{h}) = \frac{\gamma_0'(r_0)}{x_0 \gamma_0(r_0)}; \Delta_n(\bar{h}) = \bar{\Delta}_n(\bar{h}) - \Delta_n^E(\bar{h}) \Delta_n^H(\bar{h});$$

$$\gamma_{n0}(r, \bar{h}) = \frac{H_n^{(2)}(\tilde{k}_0 r)}{H_n^{(2)}(\tilde{k}_0 r_0)};$$

$$\{\gamma_{n1}(r,\bar{h}),\bar{\gamma}_{n1}(r,\bar{h})\} = \frac{H_n^{2)}(\tilde{k}_1 r)}{H_n^{(2)}(\tilde{k}_1 r_1)} + \left\{\Gamma_1 \frac{J_n(\tilde{k}_1 r)}{J_n(\tilde{k}_1 r_1)}, \bar{\Gamma}_1 \frac{J_n(\tilde{k}_1 r)}{J_n(\tilde{k}_1 r_1)}\right\};$$

$$\Gamma_1 = -\frac{J_n(\bar{x}_1)}{J_n(x_1)} \frac{H_n^{(2)}(x_1)}{H_n^{(2)}(\bar{x}_1)}; \bar{\Gamma}_1 = -\frac{J_n'(\bar{x}_1)}{J_n(x_1)} \frac{H_n^{(2)}(x_1)}{H'^{(2)}_n(\bar{x}_1)};$$

$$\widehat{k}_i^2 = k_0^2\{\varepsilon_{ri} - \bar{h}^2\}; x_i^2 = (k_0 r_0)^2\{\varepsilon_{ri} - \bar{h}^2\}; \bar{x}_1^2 = (k_0 r_1)^2\{\varepsilon_{r1} - \bar{h}^2\};$$

$$\varepsilon_{ri} = \begin{cases} \varepsilon_{r1} = \varepsilon_r & r_1 < r < r_0 \\ \varepsilon_{r0} = 1 & r > r_0 \end{cases}.$$

Here $J_n(x)$ is the Bessel function, $H_n^{(2)}(x)$ is the Hankel function of the second kind, and ε_{ri} is the related permittivity.

APPENDIX B. EVALUATION OF THE EXCITATION FIELD

The excitation field derived in terms of the diffraction problem solution for plane wave (1) incident on the Goubau line takes the form [11]

$$\mathbf{E}_z^{0,exc}(r,\varphi,z) = \sum_{n=-\infty}^{\infty} d_{nz}(\bar{h},z) e^{-in(\varphi-\beta)} \tag{B1}$$

$$\mathbf{E}_\varphi^{0,exc}(r,\varphi,z) = \sum_{n=-\infty}^{\infty} d_{n\varphi}(\bar{h},z) e^{-in(\varphi-\beta)} \tag{B2}$$

where

$$d_{nz}(\bar{h},z) = [a_n(r_0,z) + B_{n0}],$$

$$B_{n0} = -c_z^e \frac{\Delta_n^H}{k_0 r_0 \cdot \Delta} + c_\varphi^e \left[i\bar{F}_n \frac{\bar{\Delta}_n}{\Delta_n} + \frac{n\bar{h}}{x_1^2} \frac{\Delta_n^H}{\Delta_n}\right]$$

$$+c_z^m \left[-\frac{\bar{\Delta}_n}{k_0 r_0 \cdot \Delta}\right] + c_\varphi^m \left[\frac{n\bar{h}}{x_1^2} \frac{\bar{\Delta}_n}{\Delta_n} - iF_n \frac{\Delta_n^H}{\Delta_n}\right];$$

$$c_z^e = \frac{i(k_0 r_0)^2}{x_0^2} a_n'(r_0,z); \quad c_\varphi^e = \bar{a}_n(r_0,z);$$

$$c_z^m = \frac{i(k_0 r_0)^2}{x_0^2} \bar{a}_n'(r_0,z); \quad c_\varphi^m = -a_n(r_0,z);$$

$$d_{n\varphi}(\bar{h},z) = -\frac{n\bar{h}}{x_0^2} a_n(r_0,z) + \frac{i(k_0 r_0)^2}{x_0^2} \sin(\alpha) \bar{a}_n'(r_0,z)$$

$$-\frac{n\bar{h}}{x_0^2}B_{n0}+\frac{i(k_0r_0)}{x_0}\gamma'_{n0}(r_0,\bar{h})\,\bar{B}_{n0},$$

$$\bar{B}_{n0}=c_z^e\frac{\bar{\Delta}_n}{k_0r_0\Delta}+c_\varphi^e\left[-i\bar{F}_n\frac{\Delta_n^E}{\Delta_n}-\frac{1}{x_1^2}\frac{\bar{\Delta}_n^2}{\Delta_n}\right]$$

$$+c_z^m\left[\frac{\Delta_n^E}{k_0r_0\cdot\Delta}\right]+c_\varphi^m\left[i\varepsilon_{r1}F_n\frac{\bar{\Delta}_n}{\Delta_n}-\frac{n\bar{h}}{x_1^2}\frac{\Delta_n^E}{\Delta}\right];$$

$$\bar{h}=\cos(\alpha).$$

APPENDIX C. CALCULATION OF THE RIGHT HAND SIDE ELEMENTS V_i^s

For basis functions, the suggested Galerkin's scheme takes piecewise sinusoidal (PWS) functions [20]. The current density for the z- and φ-oriented PSW basis functions originated, correspondingly, at (z_i^b,φ_i^b) and (z_k^b,φ_k^b) comes to be

$$\mathbf{J}_{iz}^b(z)\;=\;J_{iz}^b(z)\mathbf{z}^0=\frac{\sin[p_z(\Delta_z-\left|z-z_i^b\right|)]}{\sin(p_z\Delta_z)}\mathbf{z}^0 \tag{C1}$$

$$\mathbf{J}_{k\varphi}^b(\varphi)\;=\;J_{k\varphi}^b(\varphi)\varphi^0=\frac{\sin[p_\varphi(\Delta_\varphi-\left|\varphi-\varphi_k^b\right|)]}{\sin(p_\varphi\Delta_\varphi)}\varphi^0 \tag{C2}$$

where $\mathbf{z}^0$ and φ^0 are the unit vectors in the z- and φ-directions, $p_z=k_0p_0$, $p_\varphi=k_0r_0p_z$, and $p_0=\sqrt{(\varepsilon_r+1)/2}$. The Fourier transform of the PWS basis and test functions is given below. For the z-oriented functions, it appears to be

$$\tilde{\mathbf{J}}_{zi}^{b(t)}(r_0,n,h)=\tilde{J}_{zi}^{b(t)}(r_0,n,h)\mathbf{z}^0=e^{iz_i^{(b,t)}h}e^{in\varphi_i^{(b,t)}}a_z^n(n)a_z^h(h)\mathbf{z}^0, \tag{C3}$$

where

$$a_z^h(\bar{h})=\frac{4}{A_z}\sin[\Delta_z(h+p_z)/2]\sin[\Delta_z(h-p_z)/2]\frac{p_z}{h^2-p_z^2}$$

$$a_z^n(n)=2\sin[\Delta_\varphi n/2)]/n\quad A_z=\sin(p_z\Delta_z).$$

For the φ-oriented functions,

$$\tilde{\mathbf{J}}_{\varphi k}^{b(t)}(r_0,n,h)=\tilde{J}_{\varphi k}^{b(t)}(r_0,n,h)\varphi^0=e^{iz_k^{(b,t)}h}e^{in\varphi_k^{(b,t)}}a_\varphi^n(n)a_\varphi^n(h)\varphi^0, \tag{C4}$$

where

$$a_\varphi^n(n)=\frac{4}{A_\varphi}\sin[\Delta_\varphi(n+p_\varphi)/2]\sin[\Delta_\varphi(n-p_\varphi)/2]\frac{p_\varphi}{n^2-p_\varphi^2}$$

$$a_\varphi^h(h)=2\sin[\Delta_\varphi h/2)]/h,\quad A_\varphi=\sin(p_\varphi\Delta_\varphi).$$

Make use of Formulas (B1), (C3), (C4) and calculate the right-hand side elements V_i^s according to (12). Then

$$V_i^z = -I_i^{zz} \sum_{n=-\infty}^{n=\infty} d_{nz}(\bar{h}, z) I_i^{z\varphi} \tag{C5}$$

$$V_i^z = -I_i^{\varphi z} \sum_{n=-\infty}^{n=\infty} d_{n\varphi}(\bar{h}, z) I_i^{\varphi\varphi} \tag{C6}$$

where

$$I_i^{zz} = e^{-i\bar{h}z_i^{(b,t)}} a_z^h(\bar{h}), \quad I_i^{z\varphi} = e^{-in\varphi_i^{(b,t)}} a_z^n(n)$$
$$I_i^{\varphi z} = e^{-i\bar{h}z_i^{(b,t)}} a_\varphi^h(\bar{h}), \quad I_i^{\varphi\varphi} = e^{-in\varphi_i^{(b,t)}} a_\varphi^n(n)$$

$\bar{h} = \cos(\alpha)$.

REFERENCES

1. *Proceedings of the 4th European Workshop on Conformal Antennas*, The Division of Electromagnetic Theory, Royal Institute of Technology, Stockholm, Sweden, May 23–24, 2005.
2. *Proceedings of the 5th European Workshop on Conformal Antennas*, University of Bristol, United Kingdom, September 10–11, 2007.
3. Wu, K. Y. and J. F. Kaufman, "Radiation pattern computation for cylindrical-rectangular microstrip antenna," *IEEE AP Symp.*, 39–42, 1983.
4. Luk, K. M., K. F. Lee, and J. S. Dahele, "Analysis of the cylindrical-rectangular patch antenna," *IEEE Trans. Antennas and Propagation*, Vol. 37, No. 2, 143–147, 1989.
5. Silva, F. C., S. B. A. Fonseca, A. J. M. Soares, and A. J. Giarola, "Analysis of microstrip antennas on circular-cylindrical substrates with a dielectric overlay," *IEEE Trans. Antennas and Propagation*, Vol. 39, No. 9, 1398–1404, 1991.
6. Habashy, T. M., S. M. Ali, and J. A. Kong, "Input impedance and radiation pattern of cylindrical-rectangular and wraparound microstrip antennas," *IEEE Trans. Antennas and Propagation*, Vol. 38, No. 6, 722–731, 1990.
7. Vecchi, G., T. Bertuch, and M. Orefice, "Analysis of cylindrical printed antennas with subsectional basis functions in the spectral domain," *Proceedings of the International Conference on*

Electromagnetics in Advanced Applications (ICEAA96), 301–304, Torino, Italy, 1996.

8. Bertuch, T., G. Vecchi, and M. Orefice, "Efficient spectral-domain simulation of conformal antennas of arbitrary shapes printed on circular cylinders," *Proceedings of the Millennium Conference on Antennas & Propagation*, 9–14, Davos, Switzerland, April 2000. (CD ROM)
9. Raffaelli, S., Z. Sipus, and P.-S. Kildal, "Analysis and measurements of conformal patch array antennas on multilayer circular cylinder," *IEEE Trans. Antennas and Propagation*, Vol. 53, No. 3, 1105–1113, 2005.
10. Erturk, V. B. and R. G. Rojas, "Efficient analysis of input impedance and mutual coupling of microstrip antennas mounted on large coated cylinder," *IEEE Trans. Antennas and Propagation*, Vol. 51, No. 4, 739–748, 2003.
11. Svezhentsev, A. Y., "Excitation of a cylindrical microstrip antenna with two symmetrically located radiating elements," *Radiophysics and Quantum Electronics*, Vol. 48, No. 6, 466–478, 2005.
12. Svezhentsev, A. Y. and G. A. E. Vandenbosch, "Efficient spatial domain moment method solution of cylindrically rectangular microstrip antennas," *IEE Proceedings, Microwaves, Antennas and Propagation*, Vol. 153, No. 4, 376–384, August 2006.
13. Svezhentsev, A. Y., "Input impedance calculation for a cylindrical microstrip antenna fed by a microstrip line," *Radiophysics and quantum electronics*, Vol. 51, No. 3, 200–209, 2008.
14. Goubau, G., "Surface waves and their applications transmission lines," *J. Appl. Phys.*, Vol. 21, No. 11, 1119–1128, 1950.
15. Stratton, J. A., *Electromagnetic Theory*, New York and London, 1941.
16. Schelkunoff, S. A., "Some equivalence theorems of electromagnetics and their application to radiation problems," *Bell Syst. Tech. Journ.*, Vol. 15, 92, 1936.
17. Harrington, R. F., *Time-Harmonic Electromagnetic Fields*, McGraw-Hill Book Company, 1961.
18. Huynh, T. and K. -F. Lee, "Single-layer single-patch wideband microstrip antenna," *Electronics Letters*, Vol. 31, No. 16, 1310–1312, 1995.
19. Svezhentsev, A. Y. and G. Vandenbosch, "Mixed-potential Green's functions for sheet electric current over metal-dielectric cylindrical structure," *Journal of Electromagnetic Waves and Applications*, Vol. 16, No. 6, 813–835, 2002.

20. Pozar, D. M., "Input impedance and mutual coupling of rectangular microstrip antennas," *IEEE Trans. Antennas and Propagation*, Vol. 30, 1191–1196, November 1982.